Vilnius University
Faculty of Physics
Institute of Photonics and Nanotechnology

Mantas Vaičiulis

INVESTIGATION OF CHARGE CARRIER DYNAMICS IN P-DOPED GaN LAYERS

Master's Thesis

Photonics and Nanotechnology
Study Programme

Student	Mantas Vaičiulis
Allowed to defend	2023-05-26
Work supervisor	Prof. Ramūnas Aleksiejūnas
Reviewer	Doc. Tomas Čeponis
Institute representative	Dr. Kazimieras Nomeika

Vilnius 2023

Contents

Introduction

Gallium nitride is a semiconductor material that became important in various fields, particularly in the production of light-emitting diodes (LEDs). By alloying GaN with other group III elements, such as indium or aluminum, the bandgap energy can be tuned in a wide range covering the visible range, enabling the manufacture of LEDs emitting blue, green, and even red light from the same material family. However, certain challenges remain that need to be overcome before these devices can reach their full potential. One such challenge is the decrease in external quantum efficiency as the indium content is increased, commonly known as the "green-gap" [1]. The cause of this phenomenon is not yet fully understood, but several theories have been proposed, including the complex character of carrier transport in disordered material and non-radiative Auger recombination of carriers [2]. Furthermore, the built-in electric field plays an important role in the carrier dynamics. The internal electric field causes spatial separation of electron and hole wavefunctions, thus limiting the probability of carrier recombination [3]. There are several strategies to mitigate this effect. The most popular one is to use thin quantum wells, but in this case one has to operate LEDs at high carrier densities, which results in IQE limiting processes. Another idea is to grow LEDs on non-polar GaN surfaces, but after many attempts it has been concluded that it is extremely difficult to obtain nonpolar InGaN of sufficient structural quality [4]. Lastly, it has been proposed to screen the field by adding additional p-doped layers into the LED structure [5]. This idea has been demonstrated to work; however, the p-type layers must be close to InGaN QW and doping with Mg requires high temperatures. This requirement leads to heating of InGaN layers during LED structure formation, which can lead to degradation of the active medium due to diffusion of indium atoms.

In this thesis, we aim to investigate p-type doping in GaN to address these issues and advance our understanding of the underlying mechanisms, ultimately contributing to the development of more efficient and reliable LED devices. Key goal is to investigate how different growth regimes impact carrier transport in the p-type GaN layers, in attempt to obtain doped p-type GaN layers at temperatures as low as possible. In particular, my objectives are (i) to compare the ambipolar diffusion coefficient, D, and lifetime of nonequilibrium carriers, τ_R, in a number of Mg-doped GaN layers, (ii) to deduce the equilibrium hole density, p_0, from the dependence of D on the carrier density, and (iii) to identify the growth conditions most suited for the growth of p-type GaN contact layers. The layers were grown at different temperatures and doped using different dopant flowrates. The measurements were conducted using light-induced transient grating (LITG) technique to determine the carrier diffusion coefficient and non-equilibrium charge carrier lifetime dependances on photoexcited carrier density, and time-integrated photoluminescence (TIPL) to determine photoluminescence quantum yield (PLQY) of the layers. Both LITG and TIPL measurement methods are non-destructive and require no contacts, which seems attractive having in mind that electrical measurements of p-type GaN is a rather complicated task.

1. Literature overview

1.1. Diffusion of charge carriers

The diffusion process in a semiconductor is described by second-order partial differential equation known as Fick's law:

$$\frac{\partial N}{\partial t} = \nabla \cdot (D \nabla N) \quad (1)$$

Where N and D represent the concentration and diffusion coefficient of the diffusant respectively. The equation is usually simplified by assuming that D is constant. With this assumption and considering one-dimensional diffusion we obtain:

$$\frac{\partial N}{\partial t} = D \frac{\partial^2 N}{\partial x^2} \quad (2)$$

In general, a charge carrier current consists of two components, namely the drift current driven by electric field and diffusion current due to density gradient. Diffusion coefficient *D* of charge carriers is the material parameter that is used to quantitatively describe the carrier diffusion. Under equilibrium conditions and in a non-degenerate semiconductor, *D* is proportional to carrier mobility μ, as it is expressed by Einstein relation:

$$D = \frac{k_B T}{e} \mu \,, \quad (3)$$

Here k_B is the Boltzmann constant, T – temperature, and e – elementary charge. Charge carrier mobility is defined as a proportionality coefficient between the carrier speed *v* and electric field *E*, $\vec{v} = \mu \vec{E}$. Mobility can also be expressed by the equation:

$$\mu = \frac{e}{m^*} \langle \tau \rangle \,, \quad (4)$$

here $\langle \tau \rangle$ is an average momentum relaxation time, m^* - the carrier effective mass. Momentum relaxation time depends on dominant carrier scattering mechanism, which depends on sample conditions. For example, carrier scattering by phonons dominates at high temperatures, scattering by other carriers is essential under high carrier densities (e.g. in metals or highly excited semiconductors), while scattering by charged impurities is typical for low temperatures.

In degenerate semiconductor, i.e. when quasi-Fermi level for a particular charge carrier approaches a respective band, *D*(*N*) starts to deviate from the approximate (3) relation. The monopolar diffusion coefficients D_e and D_h in degenerate semiconductor must be expressed as [6]:

$$D_{e/h} = D_{0\,e/h} \frac{F_{1/2}}{F_{-1/2}}, \quad (5)$$

where $D_{0\,e/h}$ is diffusion coefficient for holes or electrons at equilibrium, $F_{\pm 1/2}$ is the Fermi-Dirac integral. In computational practice Fermi-Dirac integral is described [7] as

$$F_j = \frac{1}{\Gamma(j+1)} \int_0^\infty \frac{E^j}{1 + e^{(\mathrm{E}-E_F)/\mathrm{k}_B T}} \mathrm{dE}. \quad (6)$$

Here $\Gamma()$ is the gamma function and E_F is the Fermi energy level, which can be calculated by solving the integral equation:

$$\int_0^\infty \frac{(2m^*_{e/h})^{3/2}}{2\pi^2\hbar^3} \frac{\sqrt{E}}{1 + e^{(\mathrm{E}-E_F)/\mathrm{k}_B T}} dE = n_{0\ e/h} + n_{ex}, \quad (7)$$

Where $n_{0e/h}$ and n_{ex} are the equilibrium and photoexcited carrier densities, respectively. The eq. (7) implies that equilibrium carrier density n_0 can be estimated from the dependence $D(n_{0e/h}$ and $n_{ex})$.

Ambipolar diffusion takes place when both electrons and holes are generated in the semiconductor simultaneously, for example during interband absorption. Both electrons and holes diffuse towards the area of lower concentration; however, charge carriers (usually electrons) move faster and separate from the other sign charge carriers. This charge separation gives rise to the electric field component called Dember field. This electric field binds both sign carriers not allowing for further separation, therefore the diffusivity becomes determined by the slower moving charge carriers. The ambipolar diffusion coefficient D_a is described [8] as

$$D_a = \frac{n+p}{\frac{n}{D_h} + \frac{p}{D_e}}, \quad (8)$$

where n and p are electron and hole densities, D_e and D_h are monopolar electron and hole diffusion coefficients, respectively. This relation implies that equilibrium concentration in a doped semiconductor can be measured from D_a dependency on excitation, which will be employed in this work.

1.2. Charge carrier recombination

Non-equilibrium charge carriers in semiconductors exist only temporarily. During this period free carriers can diffuse or drift in the presence of electromagnetic field, however eventually recombination still occurs. Non-equilibrium charge carriers in semiconductors recombine by either radiative or non-radiative paths, when the excess energy is released as photons or phonons, respectively. Typically for many semiconductors, the band-to-band recombination is radiative, while recombination via defect states and Auger recombination have non-radiative characteristics.

During bimolecular recombination process electron or hole travels to the other charge carrier in space where the electron then returns from the conduction band to the valence band and the hole returns from the valence band to the conduction band. The shift of the electron from the excited to the non-excited state produces energy equal to the energy difference between the two states. Since both electron and hole must meet each other in space for the process to initiate, the recombination rate R can be described [9] as

$$\mathrm{R} = B(np - n_i^2), \quad (9)$$

where B is the bimolecular recombination coefficient, which is a material parameter, n and p – non-equilibrium electron and hole densities, n_i – equilibrium charge carrier density. *B* value strongly depends on the material bandgap structure. This process has a much higher probability in direct bandgap semiconductors as it does not require a phonon for the process to take place.

Shockley-Read-Hall recombination is a process where a lattice impurity or a crystal fault traps a charge carrier of one sign, which is then followed by the trapping of a charge carrier of a different sign and the two charge carriers recombine. It can be imagined as an intermediate energy level in the bandgap. If this level is energetically closer to the conduction band, electrons get trapped more quickly than holes, and the recombination rate mainly depends on how long it takes for holes to be captured [10]. This rate can be described as

$$R_{SRH} = \frac{pn - n_i^2}{p + n + 2n_i^2 cosh\left(\frac{E_i - E_F}{k_B T}\right)} N_t \nu_{th} \sigma \tag{10}$$

where E_i and E_F are defect and Fermi energies respectively, N_t – defect density, ν_{th} – thermal drift velocity, σ – charge carrier trapping cross-section.

Auger recombination is a three particle non-radiative process. It is like bimolecular recombination as it requires a hole and electron to recombine; however, the process does not create a photon, instead the energy is transferred to a third particle. The third particle can be either an electron in the conduction band or a hole in the valence band. This third particle is then moved to a higher energy state of the corresponding band. Rate for this process can be described [11] as:

$$R_{Auger} = C_1 n^2 p + C_2 p^2 n \tag{11}$$

where C_1 and C_2 are the Auger recombination coefficients for electron-electron-hole (eeh) and electron-hole-hole (ehh) processes, respectively.

1.3. III – V group nitrides

Group III-nitrides is a family of semiconductors, composed of nitrogen and group III element including aluminum, gallium and indium. Together these elements form binary compounds AlN, GaN, InN, ternary compounds AlGaN, InGaN, InAlN as well as quaternary InGaAlN. Bandgaps for these semiconductors range from 0.8 eV for InN, 3.4 eV for GaN and 6.1 eV for AlN [12]. This broad range as well as direct bandgap makes these materials popular in optoelectronic industry as light sources as well as photovoltaic elements.

Gallium nitride has a bandgap of 3.4 eV which grants it special properties for optoelectronic devices like LEDs, especially ones operating at UV wavelength [13]. Being able to operate at room temperature makes GaN transistors ideal for power amplification in the microwave region as well as showing promising characteristics in the THz field [14]. Indium gallium nitride is a ternary alloy material produced by substituting a fraction of gallium atoms with indium atoms during the growth process [15]. By using Vegard's law, we can calculate semiconductor energy bandgap dependence on the proportion of its constituents.

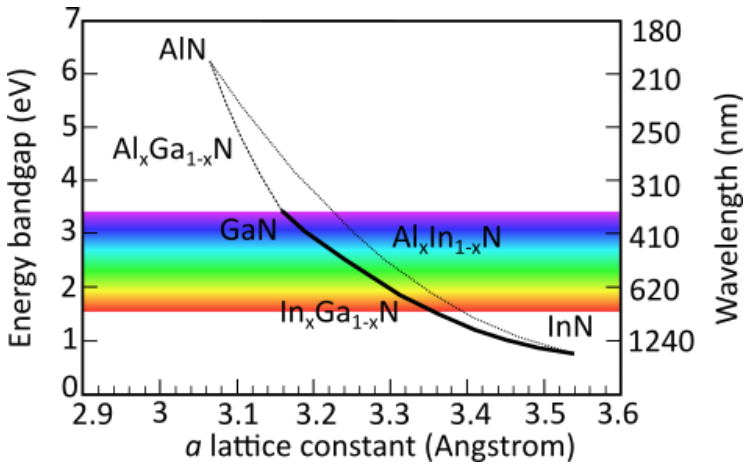

Fig. 1. Vegard's law calculation for AlN, InN and GaN products, their bandgap energy dependence on a lattice constant, adopted from [16].

Vegard's law is rarely perfectly obeyed as deviations from linear behavior are usually observed. Despite that, it gives a good starting point for engineering semiconductor structures. By changing the fraction of indium in the compound it is possible to tune the bandgap from 0.8 to 3.4 eV and in turn tune the wavelength from infrared to ultraviolet. This extreme variability throughout the visible spectrum gives rise to the possibility to create red, green and blue LEDs from a single material. The ability to create full color LEDs from a single material has been sought after property for manufacturing of LED screens. This property is no less desirable in photovoltaic industry as the bandgap is variable throughout the entire sun spectrum and could greatly increase the efficiency of solar cells. $In_xGa_{1-x}N$ with low indium content is already widely used in the industry in production of blue and ultraviolet LEDs as well as semiconductor lasers [17]. It also has been shown that low indium content increases the external quantum efficiency (EQE) of InGaN active layers [18]. To achieve single material LEDs, GaN must be doped with higher indium content of 30% or even more in order to decrease the semiconductor bandgap, in turn shifting the emission peak from UV to green region. The unwanted side effect of increased indium content, however, is a drastic drop in EQE, which would be unacceptable in large scale manufacturing of such LEDs.

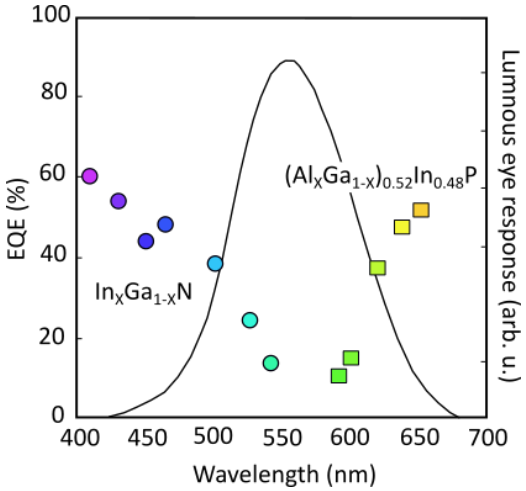

Fig. 2. EQE dependance of InGaN and AlGaInP LED on their wavelength, adopted from [19].

In Fig. 2 we can see how the external quantum efficiency changes depending on the wavelength. By increasing the indium contents and in turn increasing the emission wavelength we lose EQE as we approach the peak of luminous eye response. Similar effect can be observed in AlGaInP compounds as they too lose EQE by approaching the so called “green-gap” [20]. A proposed reason for this decrease of EQE is the dominating Auger recombination effect at high charge carrier densities [21].

1.4. Surfactant effect

It has been shown that the range in the metal/N ratio of impinging atoms allowing one to observe reflection high-energy electron diffraction (RHEED) oscillations is rather narrow [22]. A ratio smaller than 1 (indicating N-rich conditions) results in roughening of the GaN growing surface. Conversely, a ratio greater than 1 (indicating Ga- or Al-rich conditions) leads to metal accumulation, eventually resulting in droplet formation (in the case of Ga) or surface metallization (in the case of aluminum). Therefore, the optimal conditions for layer-by-layer GaN growth correspond to a slightly greater than 1 metal/N ratio.

GaN epilayers grown using In as a surfactant have shown significant improvements in both the surface morphology and the optical properties of the material. When grown with In, GaN exhibits intense band-edge luminescence, free of the component at 3.41 eV, which is characteristic of defects associated with N-rich growth conditions. Furthermore, the photoluminescence peak of the GaN film grown using In as a surfactant exhibits a low full width at half maximum (FWHM) of 5.7 meV, further indicating the excellent optical quality of the material [23]. TEM results have demonstrated that when indium is present during growth, inclined dislocations are not observed in the N-rich zone of the sample and the material is similar to GaN grown in Ga-rich conditions with no stacking faults. It is also important to note that the surfactant effect of In is observed at a growth temperature of 700 °C and above, which is sufficiently high to prevent the growth of InN. At this temperature, the surfactant effect is believed to result from the tendency of In to segregate and wet the GaN surface, combined with its low solubility in GaN. The phase diagram indicates that the solubility of InN in GaN at 700 °C is limited to 4% at thermodynamic equilibrium. In our samples no redshift of the photoluminescence was observed, indicating that no In was actually incorporated into GaN.

The doping of p-type GaN presents a significantly more intricate scenario compared to its n-type counterpart, which is a common occurrence in wide gap materials. Among the dopants employed for p-doping of GaN, magnesium has emerged as the most widely utilized, although calcium has also been proposed as a potentially shallower acceptor than Mg [24]. However, thus far, GaN layers implanted with Ca have failed to exhibit high hole concentrations comparable to those achieved with magnesium [25]. Notably, magnesium is favored for metalorganic chemical vapor deposition (MOCVD) due to the availability of high-purity organometallic sources with low vapor pressure, making them suitable for doping purposes. Early attempts to utilize magnesium as a p-dopant for GaN resulted in resistive layers with no consistently measurable hole concentrations. However, in 1988, Amano et al.

[26] observed that exposing magnesium-doped GaN samples to a low-energy electron beam (LEEBI) had a profound impact on the blue luminescence. This led to the discovery that the LEEBI treatment activated the magnesium dopant, rendering the sample p-type [27]. In 1992, Nakamura et al. proposed that the LEEBI effect could be attributed to heating the sample in a high vacuum by the electron beam [28]. They conducted thermal annealing experiments, which successfully activated Mg-doped GaN. The researchers also demonstrated that magnesium was hydrogen-compensated and that the dopant could be activated by removing hydrogen through annealing in a suitable hydrogen-free environment [29].

The resistivity of Mg-doped samples decreased when annealed at 700°C for twenty minutes, with no further decrease observed at higher temperatures. However, high annealing temperatures negatively impacted the material quality due to thermal degradation caused by nitrogen loss from the layer surface [29]. Hence, selecting an appropriate annealing temperature becomes crucial to strike a balance between efficient hydrogen diffusion and limiting sample degradation. Heat treatment for magnesium activation offers several advantages over LEEBI treatment, as it is simpler to implement and can be performed in situ within the MOCVD equipment. LEEBI treatment, on the other hand, only activates a thin layer due to the shallow penetration depth of low-energy electrons in GaN.

Regarding the incorporation of magnesium in GaN using Cp_2Mg as a precursor, Amano et al. [30, 31] reported that the incorporation is almost independent of the growth temperature within the range of 850-1040°C, indicating a lack of dopant re-evaporation from the surface. The incorporation of Mg exhibits a linear relationship with the molar flow of Cp2Mg. However, given that Mg possesses a larger covalent radius than gallium, which it replaces, the crystal quality is expected to deteriorate at high magnesium concentrations. Uniform morphology is observed up to 10^{19} atoms/cm^3, but cracks appear at higher concentrations. Unfortunately, achieving high p-type conductivity in GaN poses challenges due to the high ionization energy of Mg in GaN and the formation of inversion domains at elevated Mg concentrations. To address these difficulties, the utilization of an indium surfactant in ammonia-based molecular beam epitaxy (NH3MBE) for growing Mg-doped GaN has demonstrated higher hole concentrations at lower temperatures (740–760 °C) [32, 33]. The reduction in temperature is believed to decrease the concentration of intrinsic compensating centers and suppress the formation of nitrogen vacancies.

2. Research methodology

2.1. Samples under study

In this work, we investigate a set of magnesium-doped layers grown varying the growth temperature and the flow rate of dopant precursor. All eighteen samples were grown in Vilnius University by dr. Arūnas Kadys using AIXTRON MOVPE reactor on c-plane sapphire substrates. A 3.1 µm-thick unintentionally doped u-GaN buffer layer was deposited on sapphire, then followed by a high resistivity 2.1 µm carbon doped C-GaN layer and then a p-GaN layer.

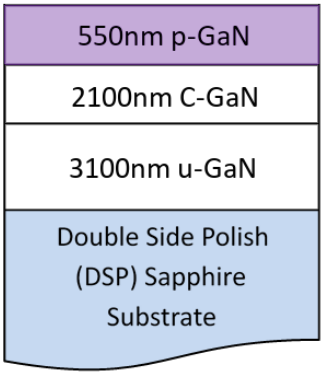

Fig. 3. The full structure of samples under study.

The magnesium doped p-GaN layers were grown at temperatures from 890 to 950°C and doped using precursor Cp_2Mg flowrates from 300 to 600 sccm. Trimethylindium (TMIn) was used as a surfactant as described in chapter 1.6. TMIn flowrates used were from 0 to 410 standard cubic centimeters per minute (sccm). Sccm is a measure of mass flow rate used to measure the quantify the flow rate of fluid, typically a gas, at standard temperature and pressure.

Table 1 (a) and (b) Samples and their growth parameters under study.

Sample #	2109	2111	2112	2113	2119	2120	2121	2126	2127
T, °C	950	950	950	950	920	920	920	920	890
q(Cp2Mg), sccm	400	500	600	300	300	400	500	600	300
q(TMIn), sccm	0	0	0	0	0	0	0	0	0

Sample #	2128	2141	2142	2143	2144	2155	2181	2182	2183
T, °C	890	890	890	950	950	950	950	920	890
q(Cp2Mg), sccm	400	500	600	500	500	500	500	500	500
q(TMIn), sccm	0	0	0	51	169	253	410	410	410

In this study, a series of sample batches were grown under various conditions to explore the growth parameters of p-type GaN. Initially, a batch of samples was grown at 950°C, focusing on the influence of the Mg precursor flowrate. Subsequently, two additional batches of samples were grown

at lower temperatures with the aim of investigating the temperature threshold for successful p-type GaN growth. Following this, a separate set of samples was grown with the introduction of an In surfactant, aimed at evaluating its efficacy and determining the optimal flowrate for promoting p-GaN growth. Finally, two more samples were grown at lower temperatures also using In surfactant to examine the potential for achieving p-GaN at reduced temperatures. Through this approach, the impact of the Mg precursor flowrate, temperature and In surfactant on p-type GaN growth could be comprehensively investigated.

2.2. Light induced transient grating

Light induced transient grating (LITG) is a variety of pump-probe technique that allows for independent determination of both carrier lifetime and diffusion coefficient. All LITG measurements were carried out using TG-Harpia (Light Conversion) spectrometer, which is an integrated device allowing for fully automated measurement. A holographic beam splitter (HBS) is used to split the pump beam into two coherent beams which then excite the sample. The excited area is hit by a probe beam, which can be delayed in relation to the pump beam by a delay line. The probe beam is diffracted from the sample and both diffracted and transmitted parts of the beam are measured. Simplified LITG measurement setup is shown in Fig. 4.

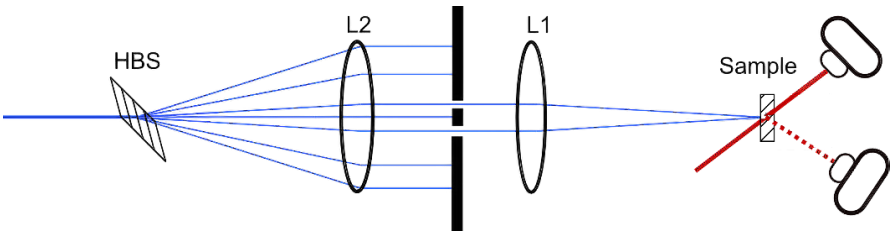

Fig. 4. Simplified view of the measurement setup.

Two coherent pump beams intersect on the sample surface at an angle θ, in turn creating an interference grating pattern with spacing

$$\Lambda = \frac{\lambda}{2\,sin\left(\frac{\Theta}{2}\right)}, \tag{12}$$

where λ – pump beam wavelength, Θ – angle between the two intersecting beams. Modulated excitation pattern generates free carriers, which then create a modulated refractive index as described by the Drude model [34]:

$$\Delta n = -\frac{e^2}{2n_0\omega^2\varepsilon_0}\left(\frac{\Delta N_e}{m_e^*} + \frac{\Delta N_h}{m_h^*}\right), \tag{13}$$

where n_0 is the refractive index of the material, ω is the circular frequency of the incident light, ΔN is excited carrier density, m^* is effective charge carrier mass. The modulated refractive index acts as a diffraction grating for the probe beam (Fig. 5).

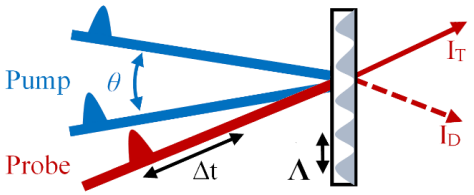

Fig. 5. Absorption of pump beam and both transmission and diffraction of probe beam.

In this measurement 355 nm wavelength was used for the pump and 1030 nm wavelength for the probe beam. The laser light was generated by a *Pharos* 30 kHz 250 fs laser and amplified using a *ORPHEUS* optical parametric amplifier (OPA). The probe laser beam was taken from the laser, whereas the pump beam was generated through the OPA and a second harmonics crystal. If the probe beam gets delayed by a delay line in relation to the pump beam, we acquire signal kinetics in time (Fig. 6).

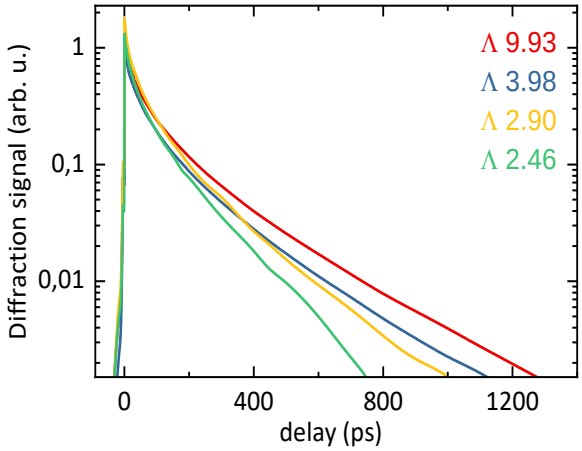

Fig. 6. Measured diffraction signal dependence on probe delay for four different grating periods.

The aim of the experiment is to determine the diffusion coefficient and lifetime on nonequilibrium carriers. We measure the signal decay in time across several grating periods to determine diffusion rate and recombination time indirectly. Each set of three or four different HBS period measurements taken with the same excitation power would look like Fig. 6, where the signal measured with higher period HBS decays slower than the signal measured when using a HBS with a lower period. By plotting the data in semilogarithmic scale, we can determine diffraction grating time τ_G by fitting the diffraction signal in time using a linear fit, as the diffraction signal η decays as an exponential function of τ_G:

$$\eta \propto exp\left(-\frac{2t}{\tau_G}\right). \tag{14}$$

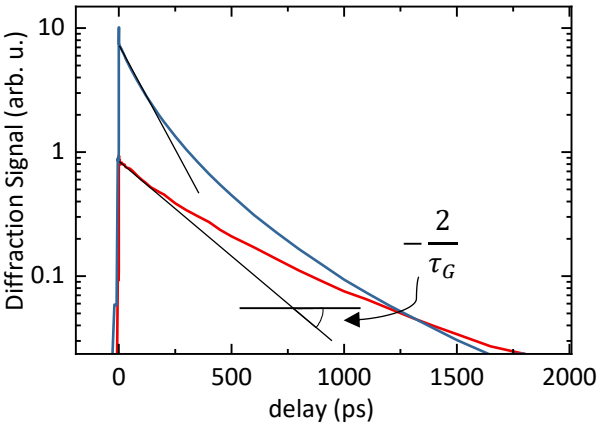

Fig. 7. Visual fit of diffraction signal dependence in time.

Diffraction signal in Fig. 7 decays due to the decay of the diffraction grating in the sample which is the result of the decaying excited charge carriers. This decay is the result of excited charge carrier recombination and diffusion processes. By fitting diffraction signal dependence on time, we can estimate characteristic diffraction grating time τ_G:

$$\frac{1}{\tau_G} = \frac{1}{\tau_R} + \frac{1}{\tau_D} = \frac{1}{\tau_R} + \frac{4\pi^2 D}{\Lambda^2} \tag{15}$$

here τ_R – recombination time and τ_D – grating decay due to carrier diffusion and Λ – interference pattern period. Equation 13 shows us, that τ_D can be changed by varying the excited carrier grating period. By doing so we can separate the τ_R and τ_D components as we plot $\frac{1}{\tau_G}$ as a function of $\frac{1}{\Lambda^2}$ (Fig.8).

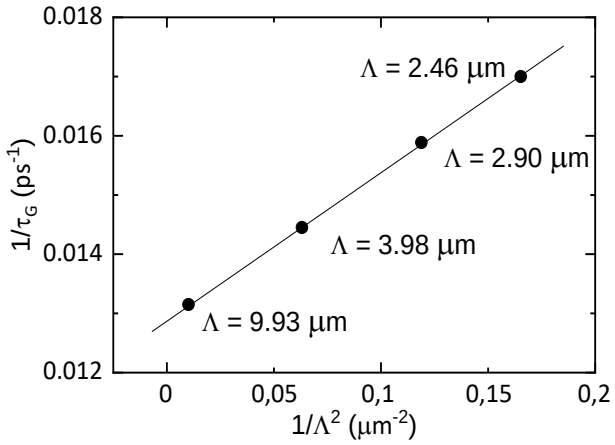

Fig. 8. Inverse grating decay time dependence on the inverse of grating period squared of a measured GaN at 120μJ/cm^2 excitation intensity.

By fitting inverse τ_G linearly, we acquire both diffusion rate as well as recombination time. In a linear fit τ_R appears as an inverse of the intercept, where D is the slope of the function divided by $4\pi^2$ (15).

2.3. Time-integrated photoluminescence measurement

Time-integrated photoluminescence (TIPL) measurement requires only one beam to excite the sample. The excited electrons jump from the valence and after the thermalization process, settle at the lowest available conduction band energy. The excited sample begins to photoluminesce, the spectra of which is collected and directed to a spectrometer. TIPL allows for the evaluation of sample's IQE by finding the ratio of absorbed and re-emitted photons. This is done by measuring the spectra in an integrating sphere using the ABC method (Fig. 9).

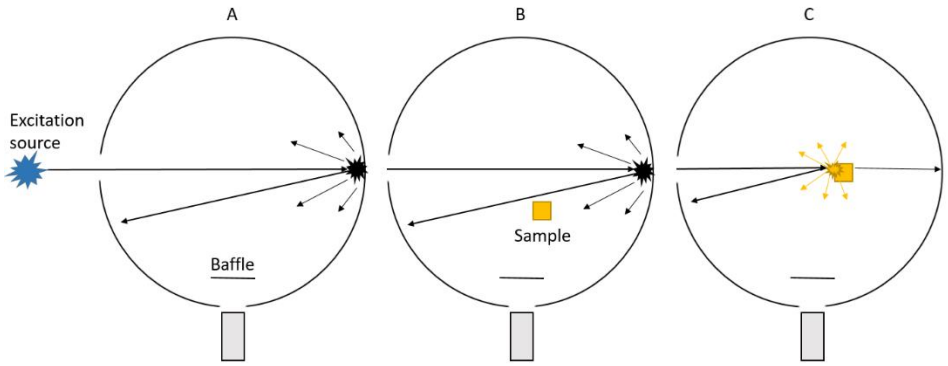

Fig. 9. Photoluminescence ABC measurement setup, A – empty sphere, B – indirect, C – direct measurement.

After acquiring the spectra for all three measurements, it is possible to calculate the photoluminescence quantum yield (PLQY). The absorption coefficient A is calculated from the integrated laser beam profile L by calculating how much the laser beam intensity drops upon direct sample excitation. Photoluminescence spectra P in indirect and direct measurements are also integrated. After acquiring these parameters PLQY can be calculated by using equations (16) and (17) [35].

$$PLQY = \frac{P_{\text{direct}} - (1 - A)P_{\text{indirect}}}{L_{\text{empty}}A} \tag{16}$$

$$A_{dir} = 1 - \frac{L_{\text{direct}}}{L_{\text{indirect}}} \tag{17}$$

Measurements in an integrating sphere for all samples were conducted twice for reference, the bulk of PL data was collected using a lens to focus more light into the glass fiber used by the spectrometer. This was done to shorten measurement duration as integrating inside the sphere, especially at low excitation fluence, would take hours and our used spectrometer (Avantes AvaSpec2048) is not cooled or externally thermally stabilized and thermal drift during long exposures would distort the signal. PL spectra gathered outside the sphere had to be corrected, in order to determine true PLQY. To do this, we plot both spectra – measured inside and outside the integrating sphere. Both spectra need to be excited using the same conditions – both the angle and the excitation

intensity must be the same. The outside spectra is then multiplied by a correction parameter in such a manner that the peak of the PL spectra outside the sphere would match the PL intensity measured inside the sphere (Fig. 10). Then this parameter is used to correct all spectra measured outside the sphere for that sample.

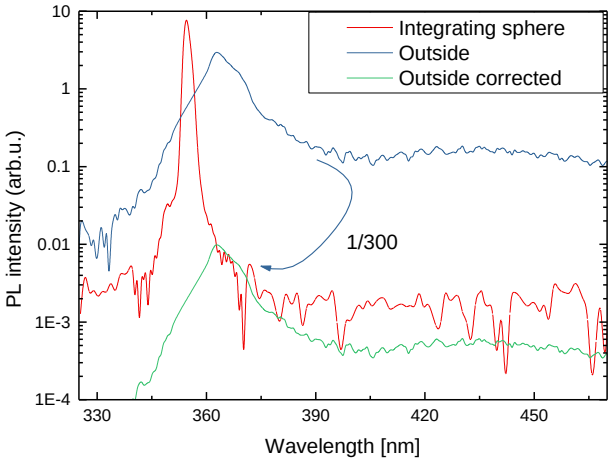

Fig. 10. Amplitude correction for spectra measured outside the integrating sphere.

The correction parameter is determined for each sample individually. Several samples were measured both inside and outside the sphere and no difference in the final PLQY was observed, except that measurements conducted outside the sphere were able to measure much wider excitation intensity region, than the measurements conducted only inside the sphere.

3. Results and discussion

3.1. Numerical modeling

The first method we employed to determine the doping concentration was numerical modeling. Equations 5 to 8, introduced in chapter 1.1, were used in Wolfram Mathematica program to perform the calculations. Material constants used in the modeling were taken from the paper by C. Li et al. [36] and are listed in Table 2.

Table 2. Parameters used for diffusion coefficient modeling.

m_e	m_h	D_e (cm2/s)	D_h (cm^2/s)
0.2 x m_0	1.87 x m_0	35	0.1

Here m_0 is electron mass, m_e and m_h are effective electron and hole masses respectively and D_e and D_h are the monopolar diffusion coefficients of electrons and holes, respectively. Density of majority carriers (n or p, depending of conductivity type) is the sole varying parameter in the modeling. The total carrier density is composed of dark, or equilibrium electron (hole) densities n_0 (p_0) and photoexcited carrier densities n_{ex}. Since band-to-band carrier photoexcitation is considered, n_{ex} is considered the same for electrons and holes.

Figure 11 shows the calculated dependencies $D_a(n_{ex})$ in p- and n- type semiconductors (a) without and (b) with degeneracy of carriers taken into account; apart from carrier densities, other parameters are the same for both cases.

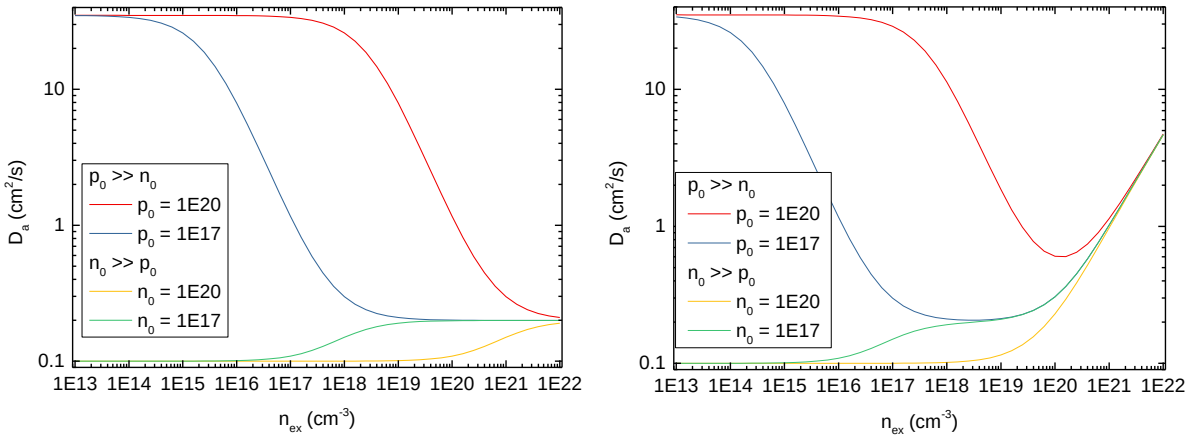

Fig. 11. Ambipolar diffusion coefficients calculated for different doping concentrations for (a) non-degenerate and (b) degenerate cases.

Without degeneracy taken into account (Fig. 11a), diffusion in the p-type semiconductor at low excitation is dominated by electron diffusion, which then decreases as excitation increases. Similarly, the ambipolar diffusion in n-type semiconductor is dominated by hole diffusion, which increases with increasing free carrier concentration. In both cases, the diffusion coefficient approaches the ambipolar value at very high n_{ex}, 0.2 cm^2/s in this example.

Degenerate semiconductors exhibit similar diffusion properties at low free carrier concentrations; however, at high excitations the onset of band degeneracy changes the previous dependence and ambipolar diffusion starts to increase with excitation. Higher doping concentrations exhibit ambipolar diffusion much later than lower doping concentrations. For example, semiconductor with 10^{17} cm^{-3} p-type doping concentration shows minimal ambipolar diffusion coefficient at 2.9×10^{18} cm^{-3} free carrier concentration, while the higher doped 10^{20} cm^{-3} model shows minima at 1.5×10^{20} cm^{-3} free carrier concentration. For n-doped samples, the higher doping concentration shows lesser impact of ambipolar diffusion and a much later increase of ambipolar diffusion coefficient. From 11a and 11b it is possible to perform the same calculations in reverse: by using the degenerate p-doped semiconductor as an example, taking the position of the ambipolar diffusion coefficient minima and doping concentration we can plot:

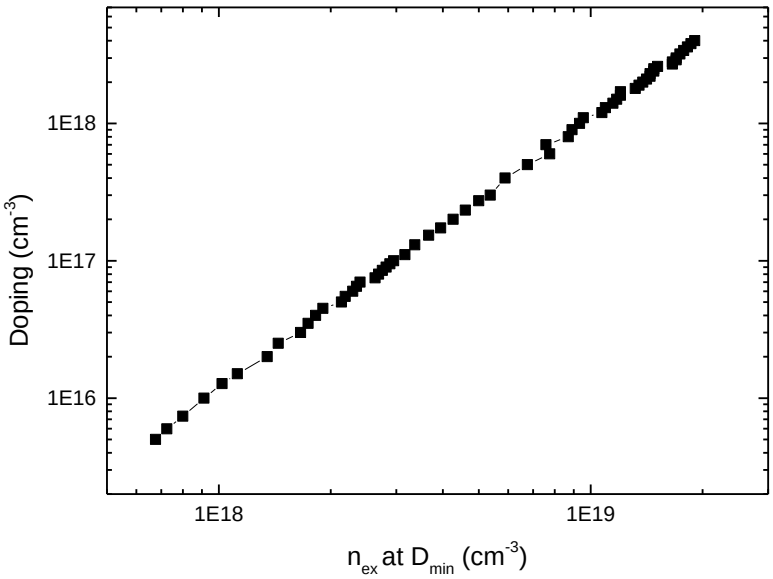

Fig. 12. p-type doping concentration dependence on free carrier concentration at ambipolar diffusion minima.

Fig. 12 shows a clear trend of diffusion coefficient minima appearing at higher free carrier concentrations with introduction of higher doping concentrations. This method was used to estimate doping concentrations for measured samples. This calculation is important as the standard method for determining doping concentration is the Hall method, however in the case of p-GaN it is difficult to produce ohmic contacts to the semiconductor and in this case could not be achieved.

3.2. LITG analysis

We begin LITG result analysis with the investigation of diffusion coefficient dependance on charge carrier concentration. Samples grown at 950^{o}C stand out from the rest as only they exhibit a decrease of diffusion coefficient $D(N)$ with the increase of charge carrier concentration (Fig. 13). This dependence can be divided into two regions. At low charge carrier densities, the diffusion coefficient

is governed by doping, as was demonstrated with modelling. At around 2×10^{18} cm^{-3} the diffusivity reaches its minima and starts to increase with excitation.

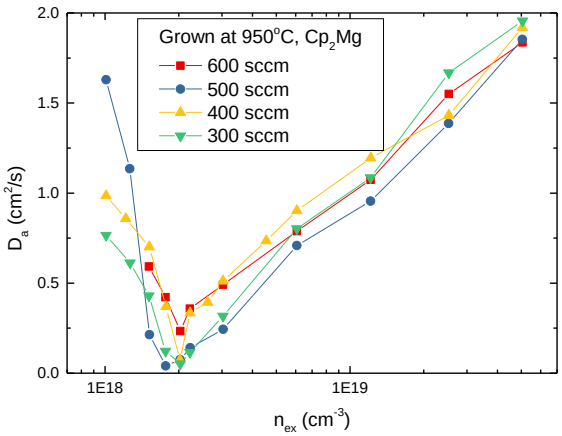

Fig. 13. Diffusion coefficient dependance on non-equilibrium carrier concentration in Samples grown at 950°C.

The first region can be described using our modeling results. If the semiconductor is of p-type, then D approaches D_e at low carrier concentrations and with the increase of non-equilibrium charge carriers the ratio value decreases. The increase of D with excitation in the second region can be attributed to carrier degeneracy, when quasi-Fermi level approaches the bands [37]. Similar result in GaN has been obtained previously, e.g. by T. Malinauskas et al. [38]. The meeting point of the two regions can theoretically give us the p-type doping density of the semiconductor as can be seen from Fig. 11(b). This is achieved by varying the doping density so that the ambipolar diffusion coefficient minimum coincides with the measured results. In the case of all samples grown at 950°C the density of free holes is estimated to be 6×10^{16} cm^{-3}.

Similar minima are not observed in the samples grown at 920 and 890°C (Fig. 14). This could be due to several reasons. Firstly, the hole density is below the threshold of sensitivity for this method. Secondly, lower growth temperature decreases the efficiency of doping by introducing more defects, which can partially compensate p-type doping as most defects and impurities act as n-type dopants [39].

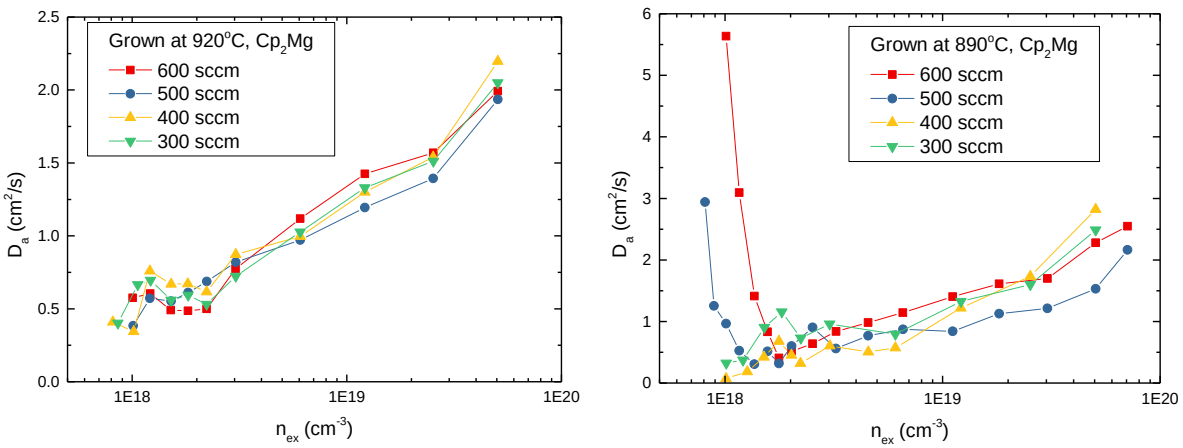

Fig. 14. Diffusion coefficient dependance on non-equilibrium carrier concentration in samples grown at (a) 920 and (b) 890°C.

The introduction of more defects could help explain the shape of diffusion coefficient dependance on carrier density in samples grown at 890°C. The three regions of hole-mobility dominated region at low carrier concentrations, the plateau region of ambipolar diffusion region at intermediate charge carrier densities and semiconductor degeneracy at high carrier concentrations are shown in Fig. 14b as well. Similar shape could be observed for samples grown at 920°C. These samples exhibit a lower ambipolar diffusion region and an earlier onset of semiconductor degeneracy.

Comparing the samples, an overall decrease of the diffusion coefficient with the increase of growth temperature can be observed. This could be explained by the deterioration of crystalline quality in terms of increasing density of scattering centers at lower growth temperatures (Fig. 15a). This can be related both to higher point defect density and higher disorder caused by introduction of Mg atoms.

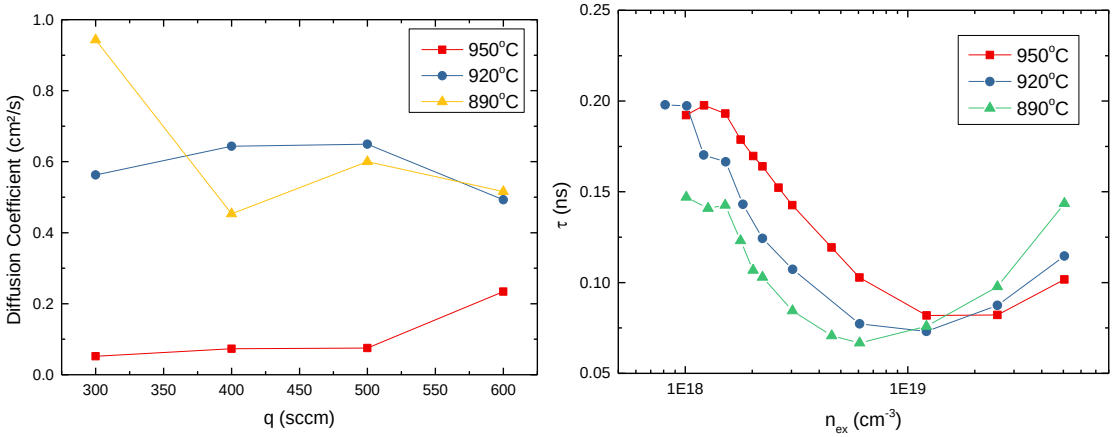

Fig. 15. (a) Diffusion coefficient dependence on precursor flow rate for samples grown at different temperatures. (b) Carrier recombination time dependance on free carrier concentration for samples grown at different temperatures at 400sccm flowrates.

Charge carrier recombination time was measured for all samples. All samples exhibited highest τ_R at low free carrier concentrations, which would decrease with higher excitation (Fig.15b). However, at free carrier concentrations of 10^{19} cm^{-3} and above, recombination time would start to increase for all samples. The reason for this increase was answered by PLQY measurements – all samples were saturating and starting to bleach at highest excitation intensities.

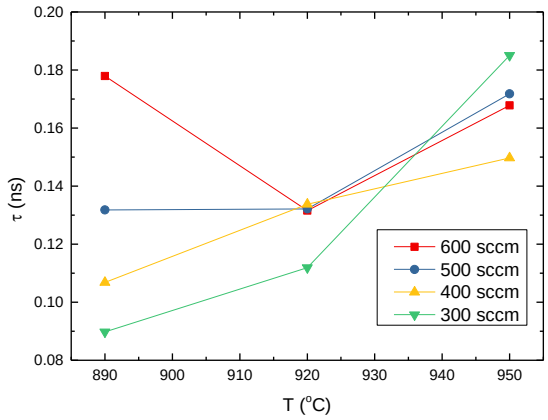

Fig. 16. Charge carrier recombination time dependance on the sample growth temperature measured at 30 μJ/cm^2 excitation intensity.

The general shape of recombination time dependance on carrier concentration did not change with the change of temperature or precursor flowrate; however, a trend of increase of τ_R with the increase of growth temperature was observed (Fig. 16). This trend seems to saturate at 400 sccm, as no increase of carrier lifetime was observed at higher flowrates. This dependence agrees with the lower point defect density in the layers grown at higher growth temperatures. It can also be noted that these lifetimes are considerably shorter than those in unintentionally doped GaN [40], confirming that adding Mg atoms facilitates nonradiative recombination.

By knowing the charge carrier lifetime τ_{R} and diffusion coefficient D, we can calculate carrier diffusion length as $L = \sqrt{D\tau_R}$ (Fig. 17). This parameter is important in further structure optimization.

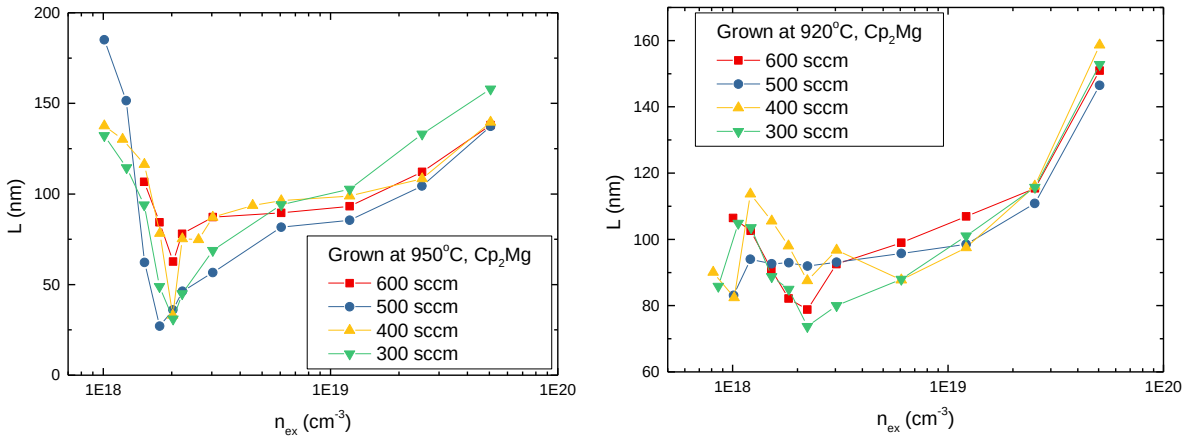

Fig. 17. Diffusion length dependance on charge carrier density for samples grown at (a) 950 and (b) 920°C.

As the carrier lifetime function for all samples follows a similar shape, the diffusion length for 950°C sample exhibits the same minima found in the diffusion coefficient graph (Fig. 13). For this reason, layer thickness for future samples should be selected to be equal or less than the carrier diffusion length at the expected carrier density of the working device. In this case, the samples grown at 950°C should be no thicker than 90nm, or even thinner if the device would be expected to mainly operate at carrier densities from 1.5 to 3 $\times$ 10^{18} cm^{-3}.

Another method used to improve the sample quality and doping concentration was using the surfactant effect of indium, described in chapter 1.4. Samples were grown using the same 500 sccm Mg precursor flowrate and different In precursor flowrates from 410 sccm to 51 sccm. Measurement results for 0 sccm sample were used from the sample batch grown at different temperatures (Fig. 13). Several samples were grown at different temperatures, from 890°c to 950°C. Similarly, the results for sample grown at 950°C using 410 sccm flowrate appear in both graphs.

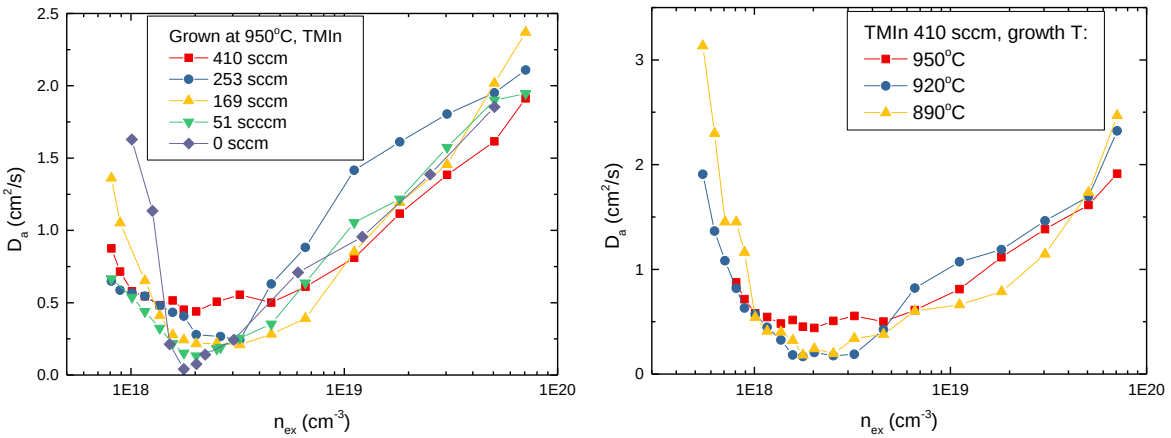

Fig. 18. Ambipolar diffusion coefficient dependance on free carrier concentration in samples grown (a) using different indium precursor flowrates and (b) at different temperatures.

From Fig. 18a we can observe a gradual shift of the diffusion coefficient minima from 2×10^{18} to 3×10^{18} cm^{-3} with the increase of In precursor flowrate, suggesting an increase of doping concentration. This effect seems to saturate and even reverse at the highest indium precursor flow rate. Additionally, to the increase of minima position, the minimal diffusion coefficient value also increases. This ambipolar diffusion coefficient increase could be explained by the increase of hole mobility. This trend can be observed in Fig. 19.

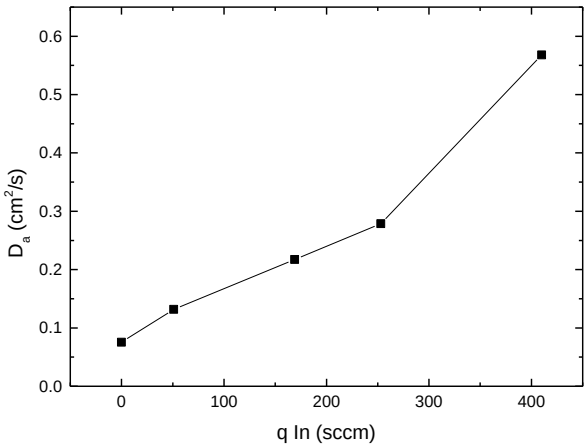

Fig. 19. Minimum ambipolar diffusion coefficient dependence on TMIn flowrate.

By using the measured diffusion minima, we can calculate the doping concentration as explained in chapter 3.1. All samples grown at 950°C with different Mg precursor flowrates and no In have been doped to 4.5×10^{16}cm^{-3}. With the introduction of In, the doping concentration is increased up to 1.2×10^{17}cm^{-3} at 253 sccm In precursor flowrate.

3.3. Photoluminescence of p-GaN layers

PL spectra gathered outside the sphere were integrated and normalized by excitation and then multiplied by a factor to match them to PLQY results gathered inside the sphere. Spectra inside the sample were treated as described in chapter 2.2. All samples showed very similar direct absorption coefficient of 90%, calculated as showed in equation (17).

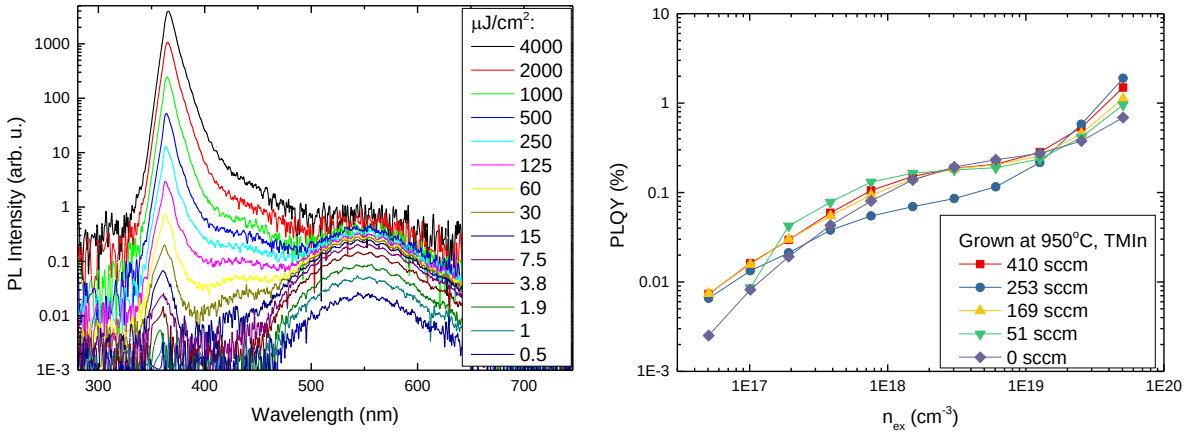

Fig. 20. (a) Example of PL spectra used for PLQY calculations. (b) Calculated PLQY for samples grown using different TMIn flowrates.

The resulting PLQY spectra for samples grown using can be seen in Fig. 20b. What seems odd at first glance – the increase of PLQY at highest free carrier densities. This could be explained by saturation and bleaching of the p-GaN layer and excitation of deeper c-GaN, shown in chapter 2.1. For this reason, no *C* parameter was used in ABC modeling in further chapter 3.4.

3.4. ABC model

A modeling method was used to investigate and quantify the recombination effects by using TIPL and LITG measurement results. Carrier density N dependent graphs were fitted using equations [41]:

$$PLQY(N) = \frac{BN}{A + BN + CN^2}, \tag{18}$$

$$\frac{1}{\tau(N)} = A + BN + CN^2. \tag{19}$$

Here, *A*, *B* and *C* denote coefficients for bimolecular, SRH and Auger recombination mechanisms respectively. τ denotes carrier decay time, obtained from LITG measurements. While these equations are attractive due to their simplicity and work quite well in simple single and multi-QW structures, their applicability in disordered LED structures is questionable. For this reason, slight modifications were used to try to account for the complexity of carrier transport and saturation of recombination coefficients, resulting in

$$PLQY(N) = \frac{B_{\mathrm{rad}}N}{A + (B_{\mathrm{rad}} + B_{\mathrm{nr}})N + CN^2}, \tag{20}$$

$$\frac{1}{\tau(N)} = A + (B_{\mathrm{rad}} + B_{\mathrm{nr}})N + CN^2. \tag{21}$$

Where B_{rad} and B_{nr} are radiative and non-radiative SRH recombination coefficients respectively. B_{nr} arises with the increase of carrier density as the closest localized states become filled and some free charge carriers above the mobility edge become much more mobile which increases the probability to reach more distant trapping states where the charge carriers recombine non-radiatively [42] resulting in lower PLQY at higher carrier densities.

$$B_{\mathrm{rad}} = \frac{B_0}{1 + \frac{N}{N_B^*}}. \tag{22}$$

Here B_0 is unsaturated recombination coefficient and N_B^* is carrier density threshold from which recombination of charge carriers becomes dominated by high-mobility non-radiative pathways. Carrier density for all samples was calculated as

$$N = (1 - R)\alpha \frac{I_0}{hv}, \tag{23}$$

where R is the reflection coefficient, α is the absorption coefficient, I_0 is the fluence of the pump beam and hv is the pump photon energy. For better accuracy α was determined separately for each sample using the integrating sphere.

An unexpected problem emerged during the measurement of PLQY – sample saturation. As a result, the uppermost layer of the sample experienced bleaching, leading to the excitation of deeper sample layers at the highest excitation intensities. While this phenomenon does not affect LITG measurements, it significantly obscures the PLQY signal, which is overshadowed by the more efficient photoluminescence emitted from the deeper layer. Consequently, measurement results exceeding 1×10^{19} cm^{-3} are presented for completeness but are not considered in the modeling process. For the same reason, *C* parameter could not be determined for any of the samples, as the influence of Auger recombination on PLQY spectra would be most visible at high free carrier concentrations.

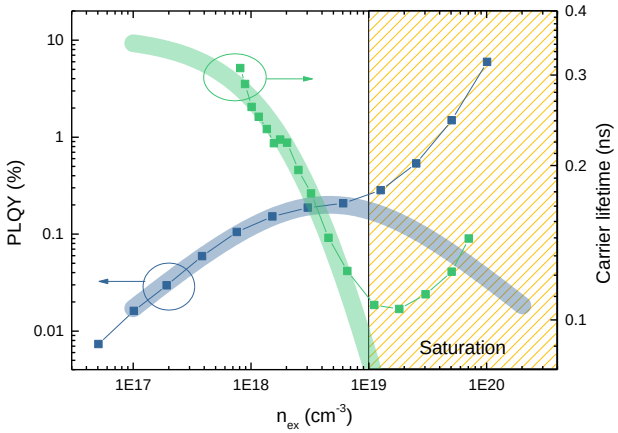

Fig. 21. Example of measured PLQY and carrier lifetimes.

The first step in ABC fitting is the determining of an approximate *A* coefficient, as it does not depend on carried density it would result as a horizontal line on the lifetime fit (Fig. 22a). By adjusting *A* we place the fit at the lifetime values at the lowest carrier density. After that we change both B_{rad} and B_{nr} as only the sum of them influences lifetime calculations (Fig. 22b). After finding the appropriate sum, so that lifetime values would be described by the fitting function we can start fitting PLQY. Since we know the sum of B_{rad} and B_{nr} we change both at the same time, such as B_{rad} describes the peak PLQY and the B_{nr} is the remainder of the previously determined sum of the two (Fig. 22c). And in the end, the SRH recombination saturation coefficient N_B^* should be adjusted as to account for the decrease of PLQY at high charge carrier densities, however due to saturation and bleaching of

investigated layer, such decrease is not visible. All these steps are done several times in order to find the values which best model both PLQY and lifetime measurements.

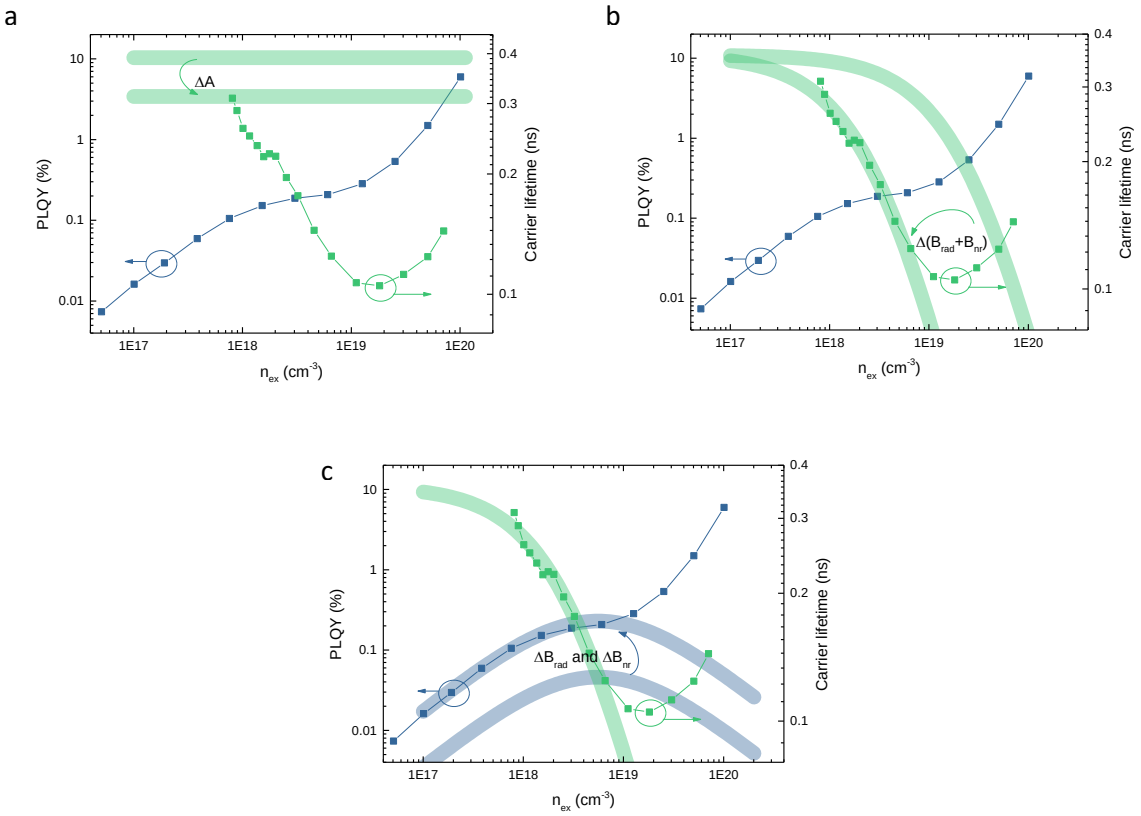

Fig. 22. The ABC modelling process used for of simultaneously fitting both PLQY and carrier lifetimes. Estimation of (a) A_0 parameter from carrier lifetime, (b) B_{sum} form carrier lifetime, (c) B_{rad} and B_{nr} ratio of B_{sum} from PLQY measurements.

It is important to observe both lifetime and PLQY fitting lines at the same time during fitting, as both functions describe the same sample and all parameters should be the exact same, given the excitation intensity did not change from one measurement to the next. The difficulty of the fitting process highly depends on the sample under study, it may not be possible to describe certain outlying points using a fitting function either due to effects inside the complex internal structure of the sample or due to errors caused by the limits of the measurement technique. Even if some outlying points are describable individually, the parameters required for that would throw off the rest of the fitting function, as attempting to adjust *A* to better fit PLQY would throw off lifetime fitting accuracy. Most problems while fitting arose at charge densities from $2x10^{17}$ to $3x10^{18}$ cm^{-3} as this region is mainly described by coefficient *A*, however no such single *A* exists where both PLQY and lifetime fitting functions would give satisfactory results. If we increase *A*, PLQY fitting function would better describe our measured results, but lifetime fitting function would agree less with measurement data and vice versa. Currently we could not measure carrier lifetimes at lower carrier densities, which also contributed to the potential fitting inaccuracies. While calculating we tried to reach a compromise between the two functions, the results for which are shown below.

Table 3. Rate coefficients of ABC model for studied samples.

Sample #	2109	2111	2112	2113	2119	2120	2121	2126	2127
A_0, s^{-1}	4.5E+09	3.5E+09	4.0E+09	3.0E+09	3.0E+09	3.5E+09	4.5E+09	3.0E+09	1.0E+10
N_b^* (cm^{-3})	3.0E+18	--	2.0E+18	1.5E+18	9.0E+19	6.0E+18	3.5E+18	1.5E+18	--
B_0 (cm^3/s)	3.0E-12	4.5E-12	8.0E-12	5.0E-12	1.5E-13	8.0E-12	5.0E-12	1.0E-11	1.0E-12
B_{sum} (cm^3/s)	7.0E-10	1.3E-09	9.0E-10	1.2E-09	3.0E-09	2.0E-09	1.5E-09	2.2E-09	7.5E-10

Sample #	2128	2141	2142	2143	2144	2155	2181	2182	2183
A_0, s^{-1}	4.5E+09	4.0E+09	3.6E+09	3.0E+09	2.5E+09	2.8E+09	2.8E+09	1.0E+09	4.5E+09
N_b^* (cm^{-3})	2.0E+18	1.0E+19	4.0E+17	1.0E+19	2.0E+19	2.5E+18	7.0E+18	1.0E+21	6.0E+18
B_0 (cm^3/s)	5.0E-12	7.0E-12	7.0E-12	5.0E-12	4.0E-12	3.5E-12	5.0E-12	2.2E-12	1.2E-12
B_{sum} (cm^3/s)	2.2E-09	1.4E-09	6.0E-10	1.0E-09	1.0E-09	1.1E-09	9.0E-10	2.3E-09	8.0E-10

Notably, all samples exhibit very similar A_0 values, with the exception of sample 2127. This could be caused by failing to determine N_B^*, which could have introduced an error in calculating other parameters of the sample. Unfortunately, it was not possible to accurately determine p-doping p_0 values using this fitting model. This could be attributed to a narrow carrier lifetime measurement window, as it was not possible to measure LITG signal at lower excitation densities due to decreasing signal-to-noise ratio. At the same time, at higher excitation densities the sample became bleached, allowing for the excitation of deeper GaN structure, which drowned out the signal. Because of this, the Auger recombination C parameter also could not be determined.

B_0 is among the most important parameters determining the PLQY of a sample. Fig. 23 shows the obtained B_0 values as a function of layer growth temperature and Mg precursor flow rate.

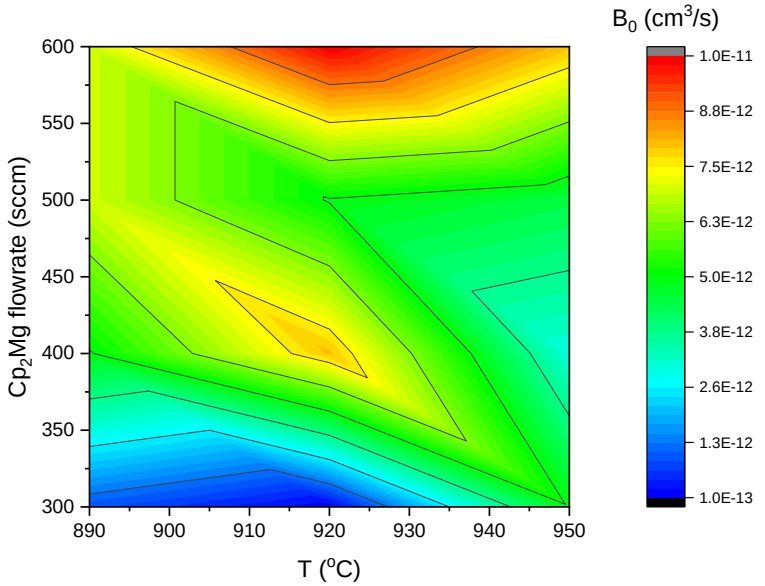

Fig. 23. Rate coefficient B_0 as a function of sample growth temperature and Mg precursor flowrate.

Samples grown at 920°C and highest Mg flowrates result in the highest coefficient of radiative SRH recombination out of all samples which is corroborated by the directly calculated PLQY, as sample 2126 showed the highest PLQY at low excitations among all samples. The unsaturated recombination coefficient B_0 and bimolecular recombination coefficient A seem to react similarly to sample growth

conditions. This result is somewhat surprising as it is believed that increasing Mg concentration degrades the luminescent properties of semiconductor. Tentatively, the increase in PLQE can be explained by larger structural disorder that causes localization of electrons and holes and, thus, increases band-to-band recombination probability.

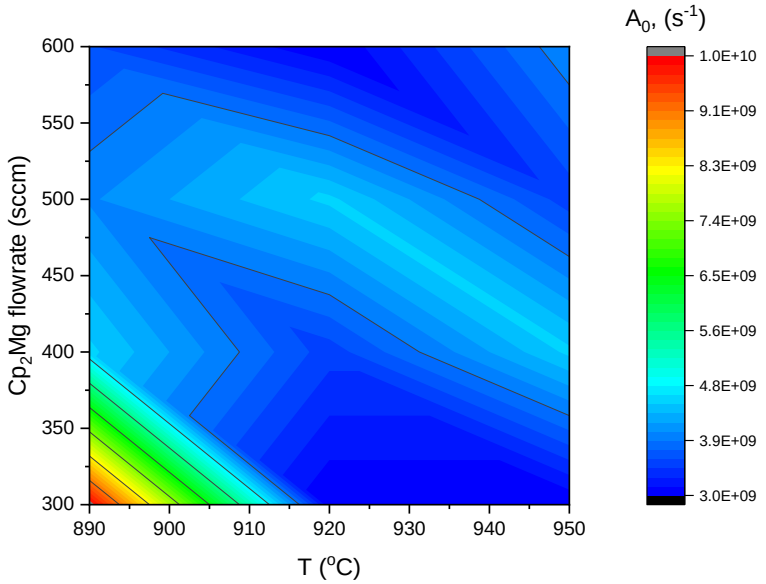

Fig. 24. Rate coefficient A_0 as a function of sample growth temperature and Mg precursor flowrate.

Coefficient *A* is directly related to the number of active recombination centers present in the sample. The ABC modeling seems to show an increased number of defects at low temperatures and decreased number of defects at high temperatures (Fig. 24), which is as expected. Notably, a slight increase in defect density occurs at the highest temperature and Cp_2Mg flowrate, which might suggest an increase of disorder within the GaN layer with the introduction of more Mg doping. All samples grown with In surfactant show lower amounts of defects than samples grown without In at the same temperatures and Mg precursor flowrates. This effect seems to saturate at 169 sccm TMIn and higher flow rates do not affect A_0 parameter.

Conclusions

i. The dependence of ambipolar diffusion coefficient on photoexcitation can be used for contactless measurement of majority carrier density in doped semiconductors. In highly doped semiconductors (when dark carrier density exceeds ~10^{17} cm^{-3}), the degeneracy of carrier bands has to be taken into account.

ii. Introduction of indium surfactant during the growth of p-GaN layers has a significant positive effect in terms of increased doping efficiency, lower defect density, and increased hole mobility.

iii. The highest used flow rates (>550 sccm) of Mg precursor Cp_2Mg results in higher bimolecular recombination rate B_0, which can be attributed to increased confining of electron-hole pairs in local minima caused by increased potential disorder.

References

[1] W. Shan et al., Band Anticrossing in GaInNAs Alloys, Physical Review Letters, 1999, DOI:10.1103/physrevlett.82.1221

[2] Y. Shen et al., Auger recombination in InGaN measured by photoluminescence, Applied Physics Letters, 91(14), 2007, DOI:10.1063/1.2785135

[3] S. Y. Karpov, Carrier localization in InGaN by composition fluctuations: implication to the "green gap", Photonics Research, 5(2), A7, 2017, DOI:10.1364/prj.5.0000a7

[4] M. Schmidt et al., High Power and High External Efficiency m-Plane InGaN Light Emitting Diodes, Japanese Journal of Applied Physics, 46(No.7), L126–L128, 2007, DOI:10.1143/jjap.46.l126

[5] T. Deguchi et al., Luminescence spectra from InGaN multiquantum wells heavily doped with Si, Applied Physics Letters, 72(25), 1998, DOI:10.1063/1.121594

[6] S. S. Li et al., Alternative formulation of generalized Einstein relation for degenerate semiconductors, Proceedings of the IEEE, 56(7), 1256–1257, 1968, DOI:10.1109/proc.1968.6561

[7] O. Koroleva et al., Approximation of Fermi-Dirac integrals of different orders used to determine the thermal properties of metals and semiconductors, Mathematica Montisnigri, 36. 37-53, 2016

[8] W. van Roosbroeck, The transport of added current carriers in a homogeneous semiconductor, Physical Review, 91, 282, 1953, DOI: 10.1103/PhysRev.91.282

[9] S. Nakamura, The Roles of Structural Imperfections in InGaN-Based Blue Light-Emitting Diodes and Laser Diodes, Science, 1998, DOI:10.1126/science.281.5379.956

[10] P. T. Landsberg et al., Recombination in semiconductors, Cambridge University Press p.616, 1991

[11] W. Shockley et al., Statistics of the Recombinations of Holes and Electrons, Physical Review 87(5) 835–842, 1952, DOI:10.1103/physrev.87.835

[12] R. A. Ferreyra et al., Group III Nitrides, Springer Handbook of Electronic and Photonic Materials, 2017, DOI:10.1007/978-3-319-48933-9_31

[13] S. N. Mohammad et al., Emerging gallium nitride-based devices, Proceedings of the IEEE, 1995, DOI:10.1109/5.469300

[14] K. Ahi, Review of GaN-based devices for terahertz operation, Optical Engineering, 2017, DOI:10.1117/1.OE.56.9.090901

[15] F. K. Yam et al., InGaN: An overview of the growth kinetics, physical properties and emission mechanisms, Superlattices and Microstructures, 2008, DOI:10.1016/j.spmi.2007.05.001

[16] B. T. Liou et al., Vegard's law deviation in band gaps and bowing parameters of the wurtzite III-nitride ternary alloys, Semiconductor Lasers and Applications II, 2005, DOI:10.1117/12.575300

[17]S. Nakamura et al., High-power InGaN/GaN double-heterostructure violet light emitting diodes, Applied Physics Letters, 1993, DOI:10.1063/1.109374

[18]A. G Bhuiyan et al., Indium nitride (InN): A review on growth, characterization, and properties, Journal of Applied Physics, 2003, DOI:10.1063/1.1595135

[19]J. Wu, When group-III nitrides go infrared: New properties and perspectives, Journal of Applied Physics, 2009, DOI:10.1063/1.3155798

[20]W. Shan et al., Band Anticrossing in GaInNAs Alloys, Physical Review Letters, 1999, DOI:10.1103/physrevlett.82.1221

[21]J. Iveland et al., Direct Measurement of Auger Electrons Emitted from a Semiconductor Light-Emitting Diode under Electrical Injection: Identification of the Dominant Mechanism for Efficiency Droop, Physical Review Letters, 110, 177406, 2013, DOI:10.1103/PhysRevLett.110.177406

[22]B. Daudin et al., Layer-by-layer growth of AlN and GaN by molecular beam epitaxy, Journal of Crystal Growth, 182(1-2), 1–5, 1997, DOI:10.1016/s0022-0248(97)00339-4

[23]F. Widmann et al., Improved quality GaN grown by molecular beam epitaxy using In as a surfactant, Applied Physics Letters, 73(18), 2642–2644, 1998, DOI:10.1063/1.122539

[24]S. Strite, GaN Core Relaxation Effects and Their Ramifications for P-Type Doping, Japanese Journal of Applied Physics, 33(Part 2, No. 5B), L699–L701, 1994, DOI:10.1143/jjap.33.l699

[25]J. W. Lee et al., Hydrogen passivation of Ca acceptors in GaN, Applied Physics Letters, 68(15), 2102–2104, 1996, DOI:10.1063/1.115598

[26]H. Amano et al., Electron beam effects on blue luminescence of zinc-doped GaN, Journal of Luminescence, 40-41, 121–122, 1998, DOI:10.1016/0022-2313(88)90117-2

[27]H. Amano, et al., P-Type Conduction in Mg-Doped GaN Treated with Low-Energy Electron Beam Irradiation (LEEBI), Japanese Journal of Applied Physics, 28(Part 2, No. 12), L2112–L2114, 1989, DOI:10.1143/jjap.28.l2112

[28]S. Nakamura et al., Thermal Annealing Effects on P-Type Mg-Doped GaN Films, Japanese Journal of Applied Physics, 31(Part 2, No. 2B), L139–L142, 1992, DOI:10.1143/jjap.31.l139

[29]S. Nakamura et al., Hole Compensation Mechanism of P-Type GaN Films, Japanese Journal of Applied Physics, 31(Part 1, No. 5A), 1258–1266, 1992, DOI:10.1143/jjap.31.1258

[30]H. Amano et al., Growth and Luminescence Properties of Mg-Doped GaN Prepared by MOVPE, Journal of The Electrochemical Society, 137(5), 1639, 1990, DOI:10.1149/1.2086742

[31]I. Akasaki et al. Photoluminescence of magnesium-doped p-type gallium nitride (GaN) and electroluminescence of gallium nitride (GaN) p-n junction LED Reviewed, Journal of Luminescence, 48-49:666, 1991

[32]C. Hurni et al., Effects of growth temperature on Mg-doped GaN grown by ammonia molecular beam epitaxy. Applied Physics Letters, 101(10), 102106, 2012, DOI:10.1063/1.4751108

[33]A. Dussaigne et al., High doping level in Mg-doped GaN layers grown at low temperature. Journal of Applied Physics, 103(1), 013110, 2008, DOI:10.1063/1.2829819

[34]H. J. Eichler et al., Laser-Induced Dynamic Gratings, Springer Series in Optical Sciences, 1986, DOI:10.1007/978-3-540-39662-8

[35]S. Leyre et al., Absolute determination of photoluminescence quantum efficiency using an integrating sphere setup, Review of Scientific Instruments 85(12), 2014, DOI:10.1063/1.4903852

[36]C. K. Li et al., Localization landscape theory of disorder in semiconductors. III. Application to carrier transport and recombination in light emitting diodes, Physical Review B, 95(14), 2017, DOI:10.1103/physrevb.95.144206

[37]S. S. Li et al., Alternative formulation of generalized Einstein relation for degenerate semiconductors, Proceedings of the IEEE, 56(7), 1256–1257, 1968, DOI:10.1109/proc.1968.6561

[38]T. Malinauskas et al., Diffusion and recombination of degenerate carrier plasma in GaN, Physica Status Solidi (c), 6(S2), S743–S746, 2009, DOI:10.1002/pssc.200880856

[39]C. G. Van de Walle, Defects and Impurities in Semiconductors, Handbook of Materials Modeling, 1877–1888, 2005, DOI:10.1007/978-1-4020-3286-8_96

[40]R. Aleksiejūnas et al., Determination of free carrier bipolar diffusion coefficient and surface recombination velocity of undoped GaN epilayers, Applied Physics Letters, 83(6), 1157–1159, 2003, DOI:10.1063/1.1599036

[41]S. Srinivasan et al., Low Stokes shift in thick and homogeneous InGaN epilayers, Applied Physics Letters, 80 (2002) 550–552, DOI:10.1063/1.1436531

[42]J. Piprek, Efficiency droop in nitride-based light-emitting diodes, Physica Status Solidi (a), 207(10), 2010, DOI:10.1002/pssa.201026149

Santrauka

Mantas Vaičiulis

Krūvininkų dinamikos tyrimas p-tipu legiruotuose GaN dariniuose

Šio darbo tikslas buvo šviesa indukuotų gardelių ir fotoliuminescencijos matavimo metodais ištirti stipriai legiruotų GaN sluoksnių ambipolinės difuzijos, krūvininkų gyvavimo trukmės ir vidinio kvantinio našumo priklausomybę nuo nepusiausvirųjų krūvininkų tankio ir skaitmeninio modeliavimo pagalba nustatyti aktyviajame sluoksnyje vykstančius rekombinacijos procesus.

Tyrimui pasirinktas InGaN yra populiari medžiaga puslaidininkinių šviestukų, šviečiančių UV ir mėlynos spalvos regione, gamyboje dėl aukšto išorinio kvantinio našumo, kuris gali siekti iki 90%. Galimybė keisti bangos ilgį ir didelis kvantinis našumas daro šią medžiagą labai patrauklią LED ekranų gamyboje, kadangi teoriškai iš vienos medžiagos galima būtų sukurti tiek mėlynus, tiek žalius ir raudonus šviestukus. Tačiau, InGaN kenčia dėl stipraus kvantinio našumo kritimo, keičiant bangos ilgį link žalios spalvos. Šis efektas, dar vadinamas žaliuoju tarpu (angl. Green-gap), yra gan gerai aprašytas, tačiau jo priežastys nėra iki galo žinomos. Viena teorija šį efektą aiškina įterptinių indžio atomų sukelta netvarka, kuri savo ruožtu sukelia puslaidininkio išsigimimus, kita teorija šį efektą grindžia viduje aktyvaus sluoksnio susiformuojančiais stipriais elektromagnetiniais laukais, kurie atplėšia krūvininkus viena nuo kito, taip mažinant skylių ir elektronų banginių funkcijų sanklotą, dėl kurios mažėja spindulinės rekombinacijos efektyvumas.

Šiems efektams nagrinėti buvo tiriami 18 stipriai magniu legiruotų GaN sluoksnių, kurių paskirtis ateityje būtų kompensuoti vidinį lauką LED struktūros aktyviajame regione. Buvo atlikti indukuotų gardelių ir fotoliuminescencijos matavimai keičiant žadinančio impulso intensyvumą nuo 0,5 iki 4000 $\mu J/cm^2$. Abu pasirinkti metodai yra ne invaziniai ir nereikalauja jokio papildomo matuojamo bandinio paruošimo, kadangi krūvininkai yra generuojami optiškai ir duomenys yra renkami matuojant zonduojantį spindulį už bandinio arba tiesiogiai bandinio išspinduliuotą šviesos spektrą.

ABC modeliavimo būdu gauti vidinio kvantinio našumo ir laisvųjų krūvininkų gyvavimo laikai sutinka su matavimų rezultatais tik prie mažų krūvininkų tankių. Didžiausią iššūkį modeliavimui kėlė didelių krūvininkų tankių sritis, kurios rezultatai, dėl bandinio struktūros, pasislėpė po signalu kylančiu iš kitų bandinio sluoksnių. Tolimesniems tyrimams ir modeliavimams reikėtų atlikti krūvininkų gyvavimo trukmės matavimus prie daug mažesnių žadinimo intensyvumų.

Iš matavimų gautos vidinio kvantinio našumo vertės parodė, kad stipriai legiruoti sluoksniai bandiniai yra ne prastesni už mažiau legiruotus bandinius. Taip pat, žemesnėje temperatūroje bandiniai buvo užauginti su mažiau defektų, nei panašūs bandiniai auginti aukštesnėje temperatūroje. Abu šie rezultatai veda prie išvados, kad šiuose bandiniuose buvo pasiektas stiprus legiravimas, kuris nepablogino bandinio parametrų.